

# Kinetic Freeze-Out Conditions and Net Baryon Density in Au+Au Collisions at $\sqrt{s_{NN}} = 7.7\text{--}39$ GeV within a Collective Flow Fireball Model

Sk Noor Alam\*

Department of Physics, Aligarh Muslim University  
Aligarh, Uttar Pradesh-202002, India

Victor Roy†

School of Physical Sciences, National Institute of Science Education and Research, Bhubaneswar 752050, India. and  
Homi Bhabha National Institute, Training School Complex,  
Anushaktinagar, Mumbai 400094, Maharashtra, India.

(Dated: March 10, 2026)

We investigate the effects of transverse and longitudinal collective flow on kinetic freeze-out conditions and net baryon density in 0–5% central Au+Au collisions at  $\sqrt{s_{NN}} = 7.7\text{--}39$  GeV within the RHIC Beam Energy Scan program. Using a covariant statistical fireball model, we fit the transverse momentum spectra of protons and positive pions from STAR data to simultaneously extract the kinetic freeze-out temperature  $T$ , baryon chemical potential  $\mu_B$ , and transverse flow velocity  $v_T$ , for three fixed longitudinal velocities  $v_z = 0.0, 0.2,$  and  $0.4$ . Longitudinal flow induces a systematic upward shift in  $T$ , spanning 143–171 MeV, 150–180 MeV, and 175–209 MeV for  $v_z = 0, 0.2,$  and  $0.4$ , respectively, arising from a kinematic degeneracy between  $v_z$  and  $T$  in the Lorentz-invariant distribution function rather than from any hardening of the  $p_T$  spectra. While temperatures extracted at  $v_z = 0$  and  $0.2$  are broadly consistent with the QCD crossover temperature  $T_c \approx 155\text{--}160$  MeV expected from lattice QCD, the values obtained at  $v_z = 0.4$  significantly exceed  $T_c$ , suggesting that the system would no longer be described by a hadron resonance gas at these conditions and indicating that large longitudinal velocities may be physically disfavored at these collision energies. The baryon chemical potential decreases monotonically from  $\mu_B \sim 420$  MeV at 7.7 GeV to  $\sim 200$  MeV at 39 GeV, independently of  $v_z$ . Reconstructing the freeze-out trajectory in the  $(\rho_B, \varepsilon)$  plane, we identify a maximum in net baryon density at  $\sqrt{s_{NN}} \lesssim 11.5$  GeV, with dynamical flow enhancing the inferred baryon compression by up to  $\sim 20\%$  relative to the static limit. These results provide refined freeze-out benchmarks for future hydrodynamic modeling and for experiments at FAIR and low-energy RHIC runs.

## I. INTRODUCTION

Mapping the phase diagram of strongly interacting matter, governed by quantum chromodynamics (QCD), across the space of temperature and chemical potentials (baryon, strangeness, etc.), and locating the critical point, represents one of the principal objectives of heavy-ion collision experiments and theoretical studies. Substantial progress has been made toward achieving this goal [1–8].

Within the QCD phase diagram [9–11], experimental data [12, 13] indicate that kinetic *freeze-out* occurs along a smooth curve in the  $(T, \mu_B)$  plane that tracks the system when inelastic reactions cease and particle yields get fixed [14, 15]. Near  $\mu_B \approx 0$ , this freeze-out line lies close to the QCD crossover band at  $T_c \simeq 155$  MeV established by lattice QCD [16], thus providing an empirical “thermometer” anchoring the phase diagram at small baryon density [17]. As  $\sqrt{s_{NN}}$  is decreased and  $\mu_B$  increases, the freeze-out line is expected to pass in the vicinity of any putative QCD critical point, making it the natural staging ground for fluctuation observables

and non-monotonic trends in Beam Energy Scan programs [18, 19]. Crucially, Randrup and Cleymans recast the freeze-out systematics into the *thermodynamic* variables constrained by conservation laws, the net baryon density  $\rho_B$  and the energy density  $\varepsilon$ . They show that  $\rho_B$  at freeze-out exhibits a clear maximum at intermediate energies (corresponding to  $\mu_B \sim 400\text{--}500$  MeV), pinpointing the region of highest net-baryon compression accessible in heavy-ion collisions and guiding the choice of collision energies at FAIR and RHIC low-energy runs [14]. In this work, we build directly on that result: by introducing collective flow into the fireball description and reevaluating the freeze-out mapping in the  $(\rho_B, \varepsilon)$  plane across  $\sqrt{s_{NN}}$ , we assess how dynamical expansion reshapes the location and prominence of the  $\rho_B$  maximum and, consequently, the proximity of freeze-out to the conjectured critical region.

The fireball formed in relativistic heavy-ion collisions is a spatially and temporally localized region of hot, dense matter composed of deconfined quarks and gluons, known as the Quark-Gluon Plasma (QGP). As the system expands and cools, it undergoes a transition into hadronic matter composed of various hadron species, well described by a Hadron Resonance Gas (HRG). There is ample evidence that both the QGP and HRG phases attain a state of local thermal equilibrium, characterized by a temperature  $T$  and chemical potential  $\mu$ . The HRG

\* noor1989phyalam@gmail.com

† victor@niser.ac.in

continues to expand until kinetic freeze-out, at which point elastic interactions cease and the momentum distributions of the constituent hadrons are fixed; it is these distributions that are ultimately recorded in detectors. As a conceptual baseline, one may treat the fireball as a static, thermalized source in the laboratory frame, from which hadrons are emitted with energies governed by the relativistic Boltzmann distribution,

$$f(E) = \lambda E e^{-E/T}, \quad (1)$$

where  $\lambda$  is a normalization constant and the factor of  $E$  arises from the momentum-space density of states,  $d^3p \propto E dE$ . In reality, however, the fireball undergoes dynamical evolution driven by internal pressure gradients, generating collective flow fields that superimpose a common expansion velocity on the underlying thermal motion. As a result, observables such as transverse-momentum spectra and particle yields carry the combined imprint of thermal and collective dynamics, and neglecting flow biases the freeze-out parameters extracted from thermal fits.

In this work we extend the analysis of Ref. [14], in which freeze-out conditions were studied in terms of  $\rho_B$  and  $\varepsilon$ , and which revealed the existence of a maximum in  $\rho_B$  at intermediate collision energies. However, that study treated the fireball as effectively static. Our aim is to investigate how the inclusion of collective flow fields modifies this picture, in particular the behavior of the freeze-out line in the  $(\rho_B, \varepsilon)$  plane as a function of  $\sqrt{s_{NN}}$ .

The paper is organized as follows. In Section II we present the theoretical formulation used to model a dynamically expanding fireball. Section III contains our main results, including fits to the transverse-momentum spectra across a range of centre-of-mass energies  $\sqrt{s_{NN}}$ , from which we extract the freeze-out temperature  $T$  and baryon chemical potential  $\mu_B$ , and subsequently map these onto the energy density  $\varepsilon$  and net baryon density  $\rho_B$  as functions of  $\sqrt{s_{NN}}$ . Section IV presents our conclusions and outlook.

Throughout this paper we adopt natural units, setting  $\hbar = c = k_B = 1$ . We choose mostly negative metric  $g_{\mu\nu} = \text{diag}(+1, -1, -1, -1)$ .

## II. MODEL OF A DYNAMIC FIREBALL

Before introducing the formulation for particle emission from a dynamically expanding thermal fireball, we first review the static fireball framework employed in Ref. [14], which serves as the baseline against which our approach is contrasted.

In the static fireball scenario, hadrons are assumed to be emitted from a thermal source following the Lorentz-invariant differential momentum distribution

$$E \frac{d^3N}{d^3p} \equiv f(E, \mathbf{p}_T, p_z), \quad (2)$$

where  $E$ ,  $\mathbf{p}_T = \sqrt{p_x^2 + p_y^2}$ , and  $p_z$  are the energy, transverse momentum, and longitudinal momentum of the particle, respectively. A more convenient kinematic variable in high-energy collisions is the rapidity  $y$ , defined as

$$y = \tanh^{-1}\left(\frac{p_z}{E}\right), \quad (3)$$

from which it follows that

$$dy = \frac{dp_z}{E}. \quad (4)$$

We further define the transverse momentum  $p_T = \sqrt{p^2 - p_z^2}$ , the transverse mass  $m_T = \sqrt{m^2 + p_T^2}$ , where  $m$  is the particle mass, and the azimuthal angle  $\varphi = \tan^{-1}(p_y/p_x)$ . The Lorentz-invariant phase-space volume element  $d^3p = dp_x dp_y dp_z$  can then be written as

$$d^3p = E dy m_T dm_T d\varphi, \quad (5)$$

with the energy expressed as  $E = m_T \cosh y$ . Substituting Eqs. (1) and (5) into Eq. (2), the differential particle spectrum for the static fireball becomes

$$\frac{d^2N}{m_T^2 dm_T dy} = \lambda \int d\varphi \cosh y e^{-\beta m_T \cosh y}, \quad (6)$$

where  $\beta = 1/T$ . The transverse-mass spectrum is obtained by integrating Eq. (6) over rapidity within the experimentally accepted window  $[y_{\text{low}}, y_{\text{up}}]$ ,

$$\frac{1}{m_T} \frac{dN}{dm_T} = \lambda \int d\varphi \int_{y_{\text{low}}}^{y_{\text{up}}} dy m_T \cosh y e^{-\beta m_T \cosh y}. \quad (7)$$

This formulation is used in Ref. [14] to evaluate the net baryon density and energy density.

To model the dynamic fireball, we adopt the covariant statistical formulation of Ref. [20]. As noted in the introduction, the fireball undergoes dynamical evolution driven by internal pressure gradients, generating collective flow fields that superimpose a common expansion velocity on the underlying thermal motion. Consider a particle with four-momentum  $p^\mu$  measured in the rest frame of a moving volume element of the fireball. We determine the transformation of the intrinsic thermal spectrum defined in the local rest frame of the moving source as seen by an arbitrary laboratory observer, expressed entirely in terms of Lorentz-covariant quantities. For a comoving volume element  $V_0$  at rest in the local frame, the Touschek invariant phase-space measure reads [20]

$$\frac{V_0 d^3p}{(2\pi)^3} e^{-E/T} \longrightarrow 2 \frac{V_\mu p^\mu}{(2\pi)^3} d^4p \delta_+(p^2 - m^2) e^{-p_\mu u^\mu / T}, \quad (8)$$

where  $\delta_+$  denotes the Dirac delta function restricted to positive energies, and  $V^\mu = V_0 u^\mu$  is the four-volume element of the flowing fireball as observed in the laboratory

frame, with  $u^\mu$  the local four-velocity field of the fireball. A standard calculation yields

$$2\delta_+(p^2 - m^2) d^4p = \frac{d^3p}{E} = m_T dm_T dy d\varphi = p_T dp_T dy d\varphi. \quad (9)$$

Adopting a cylindrical coordinate system consistent with the azimuthal symmetry of the collision geometry, the four-momentum of the particle is

$$p^\mu = (m_T \cosh y, p_T \cos \varphi, p_T \sin \varphi, m_T \sinh y). \quad (10)$$

We introduce the transverse and longitudinal rapidity variables  $y_T$  and  $y_{\parallel}$  via

$$\cosh y_T = \frac{m_T}{m} \equiv \gamma_T = \frac{1}{\sqrt{1 - v_T^2}}, \quad \sinh y_T = \frac{p_T}{m} = \gamma_T v_T, \quad (11)$$

where  $v_T^2 = v_x^2 + v_y^2$ , so that Eq. (10) becomes

$$\frac{p^\mu}{m} = (\cosh y_T \cosh y, \sinh y_T \cos \varphi, \sinh y_T \sin \varphi, \cosh y_T \sinh y). \quad (12)$$

Similarly, the four-velocity field of the fireball in cylindrical coordinates is

$$u^\mu = (\cosh y_T^{v'} \cosh y_{\parallel}^{v'}, \sinh y_T^{v'} \cos \varphi^{v'}, \sinh y_T^{v'} \sin \varphi^{v'}, \cosh y_T^{v'} \sinh y_{\parallel}^{v'}), \quad (13)$$

with  $u^\mu u_\mu = 1$ . Primed quantities ( $v'$ ,  $y_T'$ ,  $y_{\parallel}'$ ,  $\varphi'$ ) refer to the fireball velocity field, distinguishing it from the particle velocity  $v$ .

A straightforward calculation using Eqs. (12) and (13) gives

$$u_\mu p^\mu = \cosh y_T' \left[ m_T \cosh(y - y_{\parallel}') - p_T v_T' \cos(\varphi - \varphi') \right]. \quad (14)$$

Substituting Eqs. (8) and (14) into the general spectrum, we obtain the invariant spectrum, which generalises Eq. (7),

$$\frac{d^2N}{m_T^2 dm_T dy} = \frac{\lambda}{(2\pi)^3} \int d\psi \gamma_T' \left[ \cosh(y - y_{\parallel}') - \frac{p_T}{m_T} v_T' \cos \psi \right] \times \exp \left\{ -\frac{\gamma_T'}{T} \left[ m_T \cosh(y - y_{\parallel}') - p_T v_T' \cos \psi \right] \right\}, \quad (15)$$

where  $\psi = \varphi - \varphi'$  and  $\gamma_T' = \cosh y_T' = 1/\sqrt{1 - v_T'^2}$ .

Without loss of generality, we orient the coordinate system such that  $\varphi' = 0$ , i.e. the  $x$ -axis points along the transverse flow direction, giving  $\psi = \varphi$ . Since  $\cos \varphi$  is even, we may restrict the integration to  $\varphi \in [0, \pi]$  and multiply by a factor of 2. The  $\varphi$ -integral is then identified with the modified Bessel function of the first kind,

$$I_n(a) = \frac{1}{\pi} \int_0^\pi e^{a \cos \varphi} \cos(n\varphi) d\varphi, \quad (16)$$

which we evaluate numerically. Performing the azimuthal integration in Eq. (15) yields

$$\frac{d^2N}{m_T^2 dm_T dy} = \frac{\lambda \gamma_T'}{(2\pi)^2} \left[ \cosh(y - y_{\parallel}') I_0(a) - \frac{p_T}{m_T} v_T' I_1(a) \right] \times \exp \left\{ -\frac{\gamma_T' m_T \cosh(y - y_{\parallel}')}{T} \right\}, \quad (17)$$

where  $a = \gamma_T' p_T v_T'/T$ .

Equation (17) gives the invariant particle spectrum emitted from a volume element of the dynamic fireball with transverse and longitudinal flow velocities  $v_T'$  and  $v_{\parallel}'$ , as observed in the laboratory frame. The fugacity factor  $\lambda = e^{\mu_B B/T}$  accounts for the conserved baryon number  $B$  associated with each species. Since the fireball is characterised by four independent parameters, the temperature  $T$ , the baryon chemical potential  $\mu_B$ , the transverse flow velocity  $v_T'$ , and the longitudinal flow velocity  $v_{\parallel}'$  we treat all four as free parameters and determine them by fitting Eq. (17) to experimental transverse-momentum spectra.

### A. Calculation of Energy Density and Net Baryon Density

Having determined the temperature and chemical potential that best describe the experimental data at various collision energies  $\sqrt{s_{NN}}$ , we now calculate the energy and net baryon densities using standard thermodynamic relations. Specifically, we employ the grand-canonical partition function  $Z_i$  for each hadron species  $i$  to compute these quantities in Au+Au collisions at center-of-mass energies  $\sqrt{s_{NN}} = 7.7\text{--}39$  GeV. The total partition function factorizes over all species as  $Z = \prod_i Z_i$ , where  $Z_i$  depends on the temperature  $T$ , the volume element  $V$ , and the baryon, electric charge, and strangeness chemical potentials  $\mu_B$ ,  $\mu_Q$ , and  $\mu_S$ , respectively

$$\ln Z_i(T, V, \{\mu\}) = \pm \frac{VT g_i m_i^2}{2\pi^2} \sum_{n=1}^{\infty} \frac{(\pm \lambda_i)^n}{n^2} K_2\left(\frac{nm_i}{T}\right), \quad (18)$$

where the upper (lower) sign applies to bosons (fermions),  $m_i$  is the mass of species  $i$ ,  $g_i = 2J_i + 1$  is the spin degeneracy, and  $\lambda_i$  is the fugacity

$$\lambda_i(T, \{\mu\}) = \exp\left(\frac{\mu_B B_i + \mu_Q Q_i + \mu_S S_i}{T}\right), \quad (19)$$

with  $B_i$ ,  $Q_i$ , and  $S_i$  denoting the baryon number, electric charge, and strangeness of species  $i$ , respectively.

The number density of species  $i$  follows from the standard thermodynamic relation

$$n_i(T, \{\mu\}) = \frac{T}{V} \left( \frac{\partial \ln Z_i}{\partial \mu} \right)_{T,V}, \quad (20)$$

which, upon substitution of Eq. (18), yields

$$n_i(T, \{\mu\}) = \pm \frac{g_i T^3}{2\pi^2} \sum_{n=1}^{\infty} \frac{(\pm\lambda_i)^n}{n^3} \left(\frac{nm_i}{T}\right)^2 K_2\left(\frac{nm_i}{T}\right) \\ \approx \frac{g_i \lambda_i}{2\pi^2} m_i^2 T K_2\left(\frac{m_i}{T}\right) \pm \dots \quad (21)$$

Retaining only the leading ( $n = 1$ ) term in the series provides an excellent approximation for virtually all hadron species, and we adopt this approximation throughout. The net baryon density is then obtained by summing the number densities weighted by the baryon number  $B_i$ ,

$$\rho_B(T, \{\mu\}) = T \frac{\partial \ln Z}{\partial \mu_B} = \sum_i B_i n_i(T, \{\mu\}), \quad (22)$$

where the sum runs over all hadron species.

The energy density of species  $i$  is given by  $\varepsilon_i(T, \{\mu\}) = -\partial \ln Z_i / \partial \beta$ , where  $\beta = 1/T$ . Evaluating this derivative yields

$$\varepsilon_i(T, \{\mu\}) = \pm \frac{g_i T^4}{2\pi^2} \sum_{n=1}^{\infty} \frac{(\pm\lambda_i)^n}{n^4} \left(\frac{nm_i}{T}\right)^2 \\ \times \left[ K_2\left(\frac{nm_i}{T}\right) + \frac{nm_i}{T} K_1\left(\frac{nm_i}{T}\right) \right]. \quad (23)$$

Again keeping only the leading term, the energy density simplifies to

$$\varepsilon_i(T, \{\mu\}) \approx \frac{g_i \lambda_i}{2\pi^2} m_i^2 T^2 \left[ K_2\left(\frac{m_i}{T}\right) + \frac{m_i}{T} K_1\left(\frac{m_i}{T}\right) \right]. \quad (24)$$

The total energy density is  $\varepsilon = \sum_i \varepsilon_i$ . Using Eqs. (21), (22), and (24), we compute the net baryon density and energy density for Au+Au collisions across the full range of collision energies considered.

### III. RESULTS AND DISCUSSION

In this section, we present and discuss our main results. We begin by examining the best fits of Eq. (17) to the experimentally measured transverse-momentum ( $p_T$ ) spectra of identified hadrons, specifically, positive pions and protons in 0–5% central Au+Au collisions measured by the STAR Collaboration at  $\sqrt{s_{NN}} = 7.7$ –39 GeV [21]. These fits allow us to extract the normalization constant  $\lambda$ , the temperature  $T$ , the baryon chemical potential  $\mu_B$ , and the transverse flow velocity  $v_T$  for three fixed values of the longitudinal velocity  $v_z = 0, 0.2, \text{ and } 0.4$ . We then compute particle yields by integrating the fitted spectra over the rapidity range  $|y| < 0.1$  and the transverse momentum range  $0.2 < p_T < 2.0$  GeV/ $c$ , and examine their dependence on  $v_T$  at each fixed  $v_z$  in order to quantify the effect of collective flow on particle abundances.

The energy dependence of  $\mu_B$  and the  $\mu_B$  dependence of  $T$  are parametrized following Cleymans et al. [22] as

$$\mu_B(\sqrt{s_{NN}}) = \frac{d}{1 + e \sqrt{s_{NN}}}, \quad (25)$$

with  $d = 1.308 \pm 0.028$  GeV and  $e = 0.273 \pm 0.008$  GeV $^{-1}$ , and

$$T(\mu_B) = a - b \mu_B^2 - c \mu_B^4, \quad (26)$$

with  $a = 0.166 \pm 0.002$  GeV,  $b = 0.139 \pm 0.016$  GeV $^{-1}$ , and  $c = 0.053 \pm 0.021$  GeV $^{-3}$ . These parametrizations were originally obtained from thermal model fits to particle yields at chemical freeze-out, prior to the BES program. To adapt them to our dynamical model and the latest STAR data, we simultaneously refit  $T$  and  $\mu_B$  together with the transverse flow velocity  $v_T$  and the normalization  $\lambda$  using the measured proton  $p_T$  spectra. The resulting energy-dependent values, which incorporate flow-modified effective temperatures, are reported in Tables IV–VI. This reanalysis ensures thermodynamic consistency across particle species and reveals modest upward shifts in  $T$  of approximately 5–15 MeV at lower  $\sqrt{s_{NN}}$  relative to the original parametrizations of Eqs. (25) and (26), which we attribute to radial flow hardening of the  $p_T$  spectra.

#### A. Fitting the Transverse Momentum Spectra

Figures 1 and 2 show the transverse momentum spectra of protons and positive pions, respectively, fitted to STAR measurements in 0–5% central Au+Au collisions at  $\sqrt{s_{NN}} = 7.7$ –39 GeV within the rapidity range  $|y| < 0.1$ . The solid red curves represent the best fits obtained from Eq. (17) by minimizing the  $\chi^2$  per degree of freedom.

The fits describe the experimental data well across the full range of collision energies considered, as confirmed by the  $\chi^2$  per degree of freedom values for proton reported in Table I. We note that the extracted fit parameters are sensitive to the input data: even small variations in the parameter values lead to appreciable changes in the energy dependence of the spectra, underscoring the importance of a careful and consistent fitting procedure.

Table II lists the fitted parameters entering the freeze-out curve  $T(\mu_B) = a - b \mu_B^2 - c \mu_B^4$  (Eq. (26)), together with the transverse flow velocity  $v_T$ , extracted at each collision energy for three fixed values of the longitudinal velocity:  $v_z = 0.0, 0.2, \text{ and } 0.4$ . These parameters are determined by minimizing the  $\chi^2$  through least-squares fits of the dynamical fireball spectrum (Eq. (17)) to the mid-rapidity  $p_T$  distributions of identified hadrons measured by the STAR Collaboration. In each fit, the free parameters are  $T$ ,  $\mu_B$ ,  $v_T$ , and the normalization constant  $\lambda$ , while  $v_z$  is held fixed, allowing its effect on the other extracted quantities to be systematically isolated and quantified.

The spectrum of Eq. (17) is obtained by performing the azimuthal integral over  $\varphi$  in Eq. (15), where the modified Bessel functions of the first kind,

$$I_n(a) = \frac{1}{\pi} \int_0^\pi e^{a \cos \psi} \cos(n\psi) d\psi, \quad n = 0, 1, \quad \psi \equiv \varphi - \varphi'_v,$$

$\sqrt{s_{NN}}$ (GeV)	$\chi^2$	NDF
7.7	2.60346	22
11.5	2.66908	21
19.6	2.04841	22
27	2.85976	16
39	4.0128	15

TABLE I: Values of  $\chi^2$  and number of degrees of freedom from the fitted  $p_T$  spectra of protons for  $v_z = 0.2$ .

are evaluated numerically. For the fits, we integrate over the rapidity range  $|y| < 0.1$ .

$\sqrt{s_{NN}}$ (GeV)	$v_z$	$v_T$	$a$ (GeV)	$b$ (GeV $^{-1}$ )	$c$ GeV $^{-3}$
7.7	0.0	0.659±0.019	0.213±0.008	0.127±0.010	-0.050±0.012
	0.2	0.660±0.019	0.216±0.008	0.132±0.010	-0.062±0.012
	0.4	0.657±0.019	0.205±0.008	0.102±0.010	-0.08±0.014
11.5	0.0	0.659±0.019	0.214±0.008	0.133±0.010	-0.048±0.013
	0.2	0.660±0.018	0.221±0.007	0.121±0.010	-0.032±0.013
	0.4	0.657±0.051	0.216 ±0.001	0.074±0.010	-0.007±0.017
19.6	0.0	0.645±0.023	0.197±0.007	0.106±0.012	-0.047±0.020
	0.2	0.653±0.021	0.207±0.007	0.123±0.012	-0.071±0.021
	0.4	0.652±0.021	0.218±0.007	0.084±0.014	-0.049±0.023
27	0.0	0.650±0.025	0.214±0.007	0.125±0.015	-0.026±0.030
	0.2	0.652±0.025	0.217±0.008	0.121±0.016	-0.042±0.030
	0.4	0.649±0.026	0.218±0.008	0.081±0.018	-0.058±0.038
39	0.0	0.651±0.026	0.189±0.008	0.095±0.018	-0.118±0.026
	0.2	0.650±0.026	0.223±0.008	0.120±0.021	-0.034±0.049
	0.4	0.644±0.028	0.228±0.008	0.076±0.027	-0.052±0.086

TABLE II: Parameters in the expression of temperature  $T$  (Eq. (26)), along with fitted transverse velocities  $v_T$  for fixed  $v_z$ .

The values of the parameters entering the expression for the baryon chemical potential, Eq. (25), are also reported in Table III.

We now use the extracted parameters to compute the proton yield by integrating Eq. (17) over rapidity  $|y| < 0.1$  and transverse momentum  $0.425 \leq p_T \leq 1.95$  GeV, and the pion yield over  $0.275 \leq p_T \leq 1.95$  GeV (both ranges adopted directly from the STAR data), for 0–5% central Au+Au collisions at  $\sqrt{s_{NN}} = 7.7$ –39 GeV. The resulting proton yields for  $v_z = 0, 0.2, \text{ and } 0.4$  are tabulated in Table X.

Two notable features emerge from these results. First, the proton yield decreases monotonically with increasing collision energy, directly reflecting the energy dependence of *baryon stopping*. At lower  $\sqrt{s_{NN}}$ , the colliding Au nuclei are relatively opaque to one another and a significant fraction of the incoming nucleons lose most of their longitudinal momentum through multiple inelastic scatterings and come to rest near mid-rapidity, producing a large net-baryon density in the central region. This is quantitatively captured by the large values of  $\mu_B$  extracted from our fits at lower energies. As  $\sqrt{s_{NN}}$  increases, the

$\sqrt{s_{NN}}$ (GeV)	$v_z$	$v_T$	$d$ (GeV)	$e$ GeV $^{-1}$
7.7	0.0	0.659±0.019	1.319 ±0.041	0.0595±0.005
	0.2	0.660±0.019	1.241±0.037	0.048 ±0.005
	0.4	0.657±0.019	1.613±0.047	0.110±0.006
11.5	0.0	0.659±0.019	2.738±0.094	0.183 ±0.009
	0.2	0.660±0.018	1.708±0.068	0.082±0.006
	0.4	0.657±0.051	2.003 ±0.100	0.129±0.004
19.6	0.0	0.645±0.023	1.642±0.066	0.058±0.004
	0.2	0.653±0.021	1.831 ±0.074	0.08 ±0.004
	0.4	0.652±0.021	4.842±0.222	0.218 ±0.007
27	0.0	0.650±0.025	2.130±0.156	0.074 ±0.008
	0.2	0.652±0.025	2.284 ±0.150	0.081±0.007
	0.4	0.649±0.026	6.139±0.356	0.293±0.019
39	0.0	0.651±0.026	2.223 ±0.095	0.056±0.003
	0.2	0.650±0.026	2.401±0.008	0.070±0.008
	0.4	0.644±0.028	7.678±0.649	0.324±0.029

TABLE III: Parameters in the expression of baryon chemical potential (Eq. (25)), along with fitted transverse velocities  $v_T$  for fixed  $v_z$ .

$\sqrt{s_{NN}}$ (GeV)	$T$ (GeV)	$\mu_B$ (GeV)
7.7	0.143	0.905
11.5	0.140	0.880
19.6	0.151	0.771
27	0.158	0.710
39	0.171	0.694

TABLE IV: Values of  $T$  and  $\mu_B$  for  $v_z = 0$

$\sqrt{s_{NN}}$ (GeV)	$T$ (GeV)	$\mu_B$ (GeV)
7.7	0.150	0.907
11.5	0.147	0.878
19.6	0.159	0.767
27	0.166	0.718
39	0.180	0.643

TABLE V: Values of  $T$  and  $\mu_B$  for  $v_z = 0.2$ .

$\sqrt{s_{NN}}$ (GeV)	$T$ (GeV)	$\mu_B$ (GeV)
7.7	0.175	0.872
11.5	0.172	0.806
19.6	0.186	0.752
27	0.193	0.688
39	0.209	0.562

TABLE VI: Values of  $T$  and  $\mu_B$  for  $v_z = 0.4$ .

nuclei become progressively more transparent, and the incoming baryons largely retain their longitudinal momentum, being carried to forward and backward rapidities ( $|y| \gg 0$ ) while leaving a nearly baryon-free region at mid-rapidity. Consequently,  $\mu_B \rightarrow 0$  at high energies, and the proton yield at mid-rapidity diminishes accordingly. The increasing availability of center-of-mass energy also drives copious production of quark-antiquark

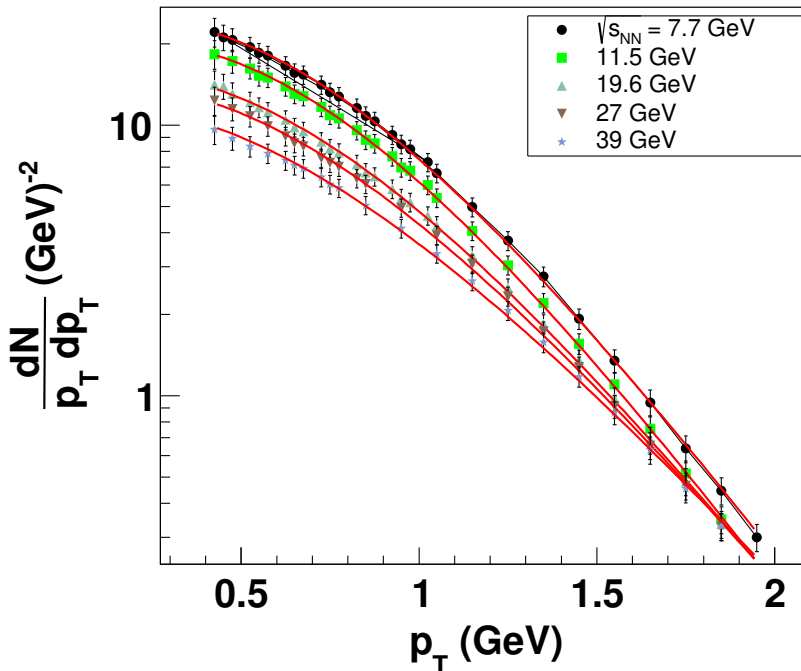


FIG. 1: (Color online) Midrapidity ( $|y| < 0.1$ ) transverse momentum spectra for positive protons in Au+Au collisions at  $\sqrt{s_{NN}} = 7.7$  to 39 GeV for 0-5% centrality with longitudinal velocity  $V_z = 0.0$  of the dynamic fireball. The red lines are fits using Eq.(17) [21].

pairs, manifesting as a sharp rise in pion yields with  $\sqrt{s_{NN}}$ , as clearly seen in Fig. 2. Thus, as the collision energy increases, the character of particle production at mid-rapidity transitions from baryon-dominated to meson-dominated, a signature of the approach toward net-baryon transparency.

Second, the proton yield is found to be essentially independent of the longitudinal fireball velocity  $v_z$ . This can be understood as follows. The net-baryon content at mid-rapidity is established during the very early, pre-equilibrium stage of the collision through baryon stopping, well before any collective flow develops. Collective longitudinal flow, characterized by  $v_z$ , acts as a subsequent rigid rapidity boost of the expanding fireball. For the narrow rapidity window  $|y| < 0.1$  considered here, such a boost shifts the rapidity distribution by  $\Delta y \sim \tanh^{-1}(v_z)$ , but since the net-baryon rapidity distribution is broad and approximately flat near mid-rapidity at these energies, the integrated yield within this small window remains largely unaffected. In other words, the conserved baryon charge within  $|y| < 0.1$  is insensitive to the collective longitudinal motion of the fireball, as long as  $v_z$  remains moderate, consistent with our chosen values of  $v_z \leq 0.4$ .

Using the parameters from Tables II and III in Eqs. (26) and (25), we extract the temperature  $T$  and baryon chemical potential  $\mu_B$  at each collision energy for 0-5% central Au+Au collisions and for each of the three fixed longitudinal velocities  $v_z = 0.0, 0.2, \text{ and } 0.4$ . The

resulting  $T-\mu_B$  freeze-out points are displayed in Fig. 3.

Several trends are immediately apparent. As  $\sqrt{s_{NN}}$  increases,  $\mu_B$  decreases monotonically, consistent with the picture of increasing nuclear transparency and diminishing net-baryon stopping at mid-rapidity discussed above. Simultaneously,  $T$  increases with  $\sqrt{s_{NN}}$ , reflecting the larger energy density deposited in the collision zone at higher energies. Together, these trends trace a freeze-out curve in the  $T-\mu_B$  plane that moves from the high- $\mu_B$ , low- $T$  region (low energies) toward the low- $\mu_B$ , high- $T$  region (high energies), consistent with the parametrization of Cleymans et al. [22] and the broader systematics of chemical freeze-out across a wide range of beam energies.

A second important feature visible in Fig. 3 is the systematic upward shift in the extracted  $T$  as  $v_z$  increases, at all collision energies. This effect is not a consequence of longitudinal flow hardening the  $p_T$  spectra, longitudinal motion is along the beam axis and cannot directly transfer momentum into the transverse plane. Rather, the origin is kinematic: in our model, the distribution function depends on the Lorentz-invariant product  $p^\mu u_\mu$ , where  $u^\mu$  is the four-velocity of the fluid element. When  $v_z \neq 0$ , the longitudinal component of  $u^\mu$  is nonzero, and the effective energy of a particle as seen in the fluid rest frame receives a contribution from the longitudinal motion through the Lorentz factor  $\gamma_z = (1 - v_z^2)^{-1/2}$ . Consequently, at fixed observed  $p_T$  and rapidity  $y$ , the argument of the thermal distribution is modified relative

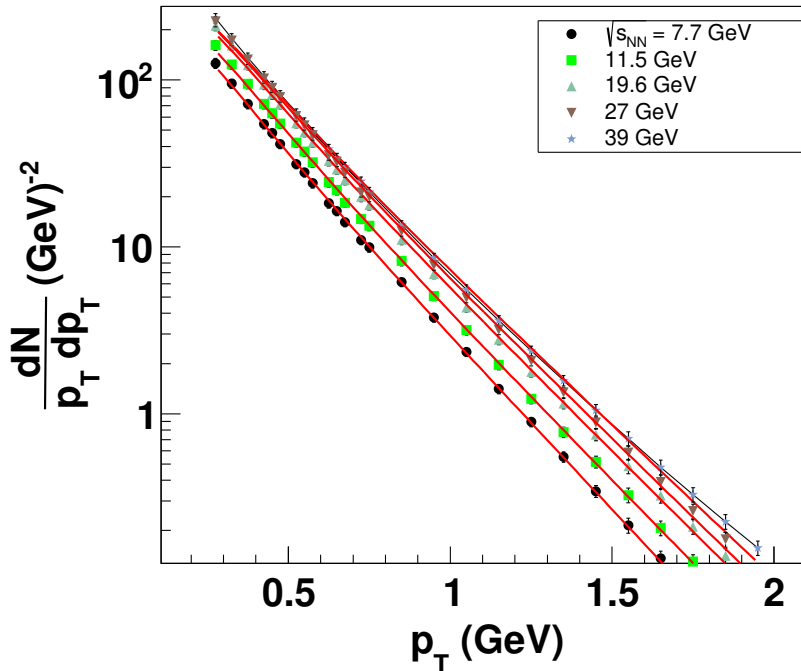


FIG. 2: (Color online) Midrapidity ( $|y| < 0.1$ ) transverse momentum spectra for positive pions in Au+Au collisions at  $\sqrt{s_{NN}} = 7.7$  to 39 GeV for 0-5% centrality with longitudinal velocity  $V_z = 0.0$  of the dynamic fireball. The red lines are fits using Eq.(17) [21].

to the  $v_z = 0$  case. To reproduce the same observed spectrum, the least-squares fit compensates by returning a higher value of  $T$ . This represents a genuine degeneracy in the model between the longitudinal collective velocity and the thermal temperature, and shows the importance of treating  $v_z$  as an explicit free parameter rather than absorbing its effects implicitly into an effective temperature. Notably,  $\mu_B$  is comparatively insensitive to  $v_z$ , since the net-baryon content at mid-rapidity is governed primarily by the initial stopping dynamics rather than by the subsequent collective expansion.

Using the extracted  $T$  and  $\mu_B$  at each collision energy, we compute the net baryon density via Eq. (22) and the energy density via Eq. (24), setting  $\mu_S = \mu_Q = 0$  and employing full quantum statistics throughout. The results are displayed in Fig. 4 and tabulated in Tables VII–IX.

The net baryon density is largest at  $\sqrt{s_{NN}} = 7.7$  GeV and decreases monotonically with increasing collision energy. This behavior directly reflects the energy dependence of  $\mu_B$ : as  $\sqrt{s_{NN}}$  increases, the decreasing degree of baryon stopping leads to a smaller net-baryon density at mid-rapidity, and correspondingly smaller  $\mu_B$ . At higher collision energies, freeze-out therefore occurs in a more baryon-dilute environment characterized by low  $\mu_B$  and low net baryon density, but at a higher thermal temperature, consistent with the general systematics of chemical freeze-out across a wide range of beam energies.

The extracted freeze-out temperatures span the ranges 143–171 MeV for  $v_z = 0.0$ , 150–180 MeV for  $v_z = 0.2$ ,

and 175–209 MeV for  $v_z = 0.4$ , across the collision energy range  $\sqrt{s_{NN}} = 7.7$ –39 GeV. The systematic upward shift of approximately 30–40 MeV per unit increment in  $v_z$  is consistent with the kinematic degeneracy between longitudinal collective motion and thermal temperature discussed above: the larger the longitudinal velocity of the fireball, the larger the compensation in  $T$  required by the fit to reproduce the observed spectra. Importantly, these temperatures are all in the range expected for hadron gas freeze-out and are broadly consistent with lattice QCD estimates of the QCD crossover transition temperature  $T_c \approx 155$ –160 MeV, particularly at the higher collision energies where  $\mu_B$  is small.

$\sqrt{s_{NN}}$ (GeV)	$\rho_B$ ( $fm^{-3}$ )	$\varepsilon$ ( $MeV/fm^{-3}$ )
7.7	0.0438	53.732
11.5	0.0341	41.597
19.6	0.0227	29.14
27	0.0193	25.727
39	0.0276	38.438

TABLE VII: Values of  $\varepsilon$  and  $\rho_B$  for  $v_z = 0$

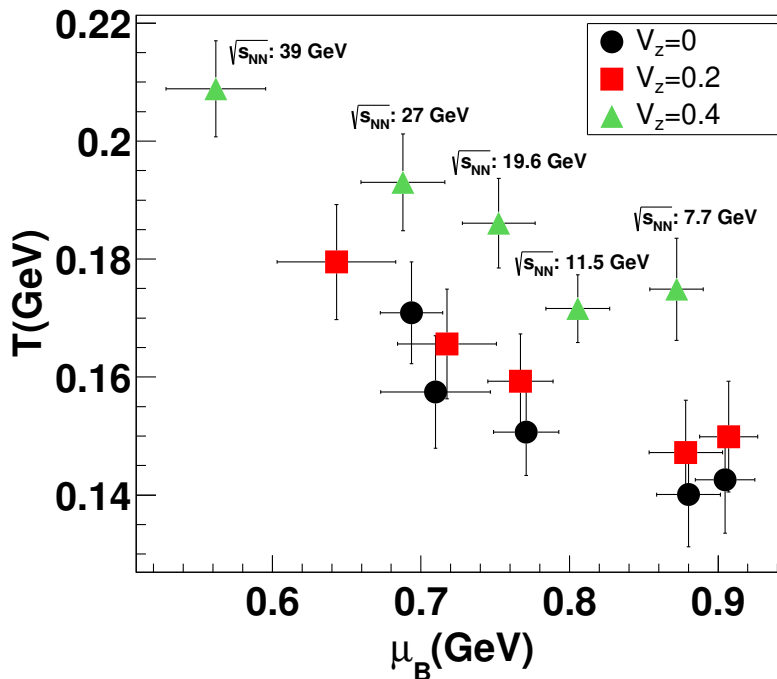


FIG. 3: (Color online) Baryon chemical potential vs temperature for three longitudinal velocities  $v_z = 0$  (black circles),  $v_z = 0.2$  (red squares), and  $v_z = 0.4$  (green triangles).

$\sqrt{s_{NN}}$ (GeV)	$\rho_B$ ( $fm^{-3}$ )	$\varepsilon$ ( $MeV/fm^{-3}$ )
7.7	0.0548	68.869
11.5	0.0418	52.215
19.6	0.0295	38.846
27	0.0268	36.405
39	0.0274	39.885

TABLE VIII: Values of  $\varepsilon$  and  $\rho_B$  for  $v_z = 0.2$

$\sqrt{s_{NN}}$ (GeV)	$\rho_B$ ( $fm^{-3}$ )	$\varepsilon$ ( $MeV/fm^{-3}$ )
7.7	0.0871	117.787
11.5	0.0542	73.471
19.6	0.0608	86.569
27	0.0527	77.863
39	0.0443	72.734

TABLE IX: Values of  $\varepsilon$  and  $\rho_B$  for  $v_z = 0.4$

#### IV. CONCLUSIONS AND OUTLOOK

In this study, we have systematically investigated kinetic freeze-out conditions in Au+Au collisions at  $\sqrt{s_{NN}} = 7.7$ –39 GeV using a covariant statistical fireball model that explicitly incorporates both transverse and longitudinal collective flow, following the parametrization of Randrup et al. [14]. By fitting the transverse momentum spectra of protons and positive pions measured by the STAR Collaboration in 0–5% central collisions within the rapidity range  $|y| < 0.1$ , we simultaneously

$\sqrt{s_{NN}}$ (GeV)	$v_z$	Proton's yield
7.7	0.0	8.498
	0.2	8.496
	0.4	8.483
11.5	0.0	6.992
	0.2	6.994
	0.4	6.994
19.6	0.0	5.466
	0.2	5.465
	0.4	5.460
27	0.0	4.916
	0.2	4.912
	0.4	4.900
39	0.0	4.180
	0.2	4.175
	0.4	4.160

TABLE X: The protons yield at different energy from  $\sqrt{s_{NN}} = 7.7$ –39 GeV for different longitudinal velocities in Au+Au collisions.

extracted the freeze-out temperature  $T$ , baryon chemical potential  $\mu_B$ , transverse flow velocity  $v_T$ , and normalization  $\lambda$  for three fixed values of the longitudinal velocity  $v_z = 0.0, 0.2, \text{ and } 0.4$ , using  $\chi^2$  minimization.

Our principal findings are as follows. The inclusion of longitudinal collective flow leads to a systematic upward shift in the extracted freeze-out temperature; the fitted  $T$  spans 143–171 MeV for  $v_z = 0$ , 150–180 MeV for  $v_z = 0.2$ , and 175–209 MeV for  $v_z = 0.4$ , across

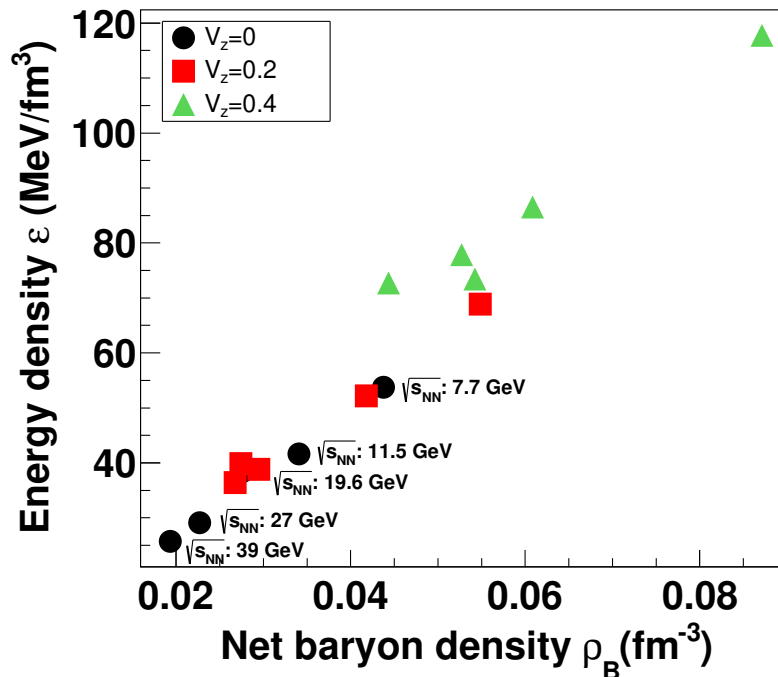


FIG. 4: (Color online) The Hadronic freeze-out points in the  $\rho_B$ - $\epsilon$  phase plane as obtained in the statistical model with the values of  $\mu_B$  and  $T$  obtained from the fitting of the transverse momentum of proton at the different STAR energies with different dynamic fireball's longitudinal velocities.

the BES energy range. This shift is not a consequence of longitudinal flow hardening the  $p_T$  spectra, which it cannot, as longitudinal motion does not directly transfer momentum into the transverse plane but rather reflects a kinematic degeneracy: the longitudinal component of the fluid four-velocity modifies the Lorentz-invariant phase-space factor  $p^\mu u_\mu$  in the distribution function, and the fit compensates by returning a higher  $T$ . The baryon chemical potential  $\mu_B$ , by contrast, is comparatively insensitive to  $v_z$ , as it is governed primarily by the initial baryon stopping dynamics rather than by subsequent collective expansion.

It is important to note that while the freeze-out temperatures extracted for  $v_z = 0.0$  and  $v_z = 0.2$  are broadly consistent with the QCD crossover temperature  $T_c \approx 155$ – $160$  MeV estimated from lattice QCD, the values obtained at  $v_z = 0.4$  significantly exceed  $T_c$ , reaching up to  $\sim 209$  MeV at the highest collision energies. Above  $T_c$ , the system is no longer expected to exist as a hadron resonance gas, rather, it transitions into a deconfined quark-gluon plasma (QGP), where the HRG model underlying our statistical fireball framework is no longer applicable. This represents an important internal consistency check: the extraction of freeze-out parameters within an HRG-based model is only physically meaningful when the resulting temperatures satisfy  $T \lesssim T_c$ . The fact that  $v_z = 0.4$  systematically violates this bound suggests that such large longitudinal velocities are physically disfavored at these collision energies, and that the  $T$ -

$v_z$  kinematic degeneracy is driving  $T$  into an unphysical regime. The results at  $v_z = 0.0$  and  $v_z = 0.2$ , where  $T$  remains below or near  $T_c$ , are therefore the most physically reliable extractions from the present analysis.

Across all values of  $v_z$ , the freeze-out trajectory in the  $T$ - $\mu_B$  plane is consistent with the parametrization of Cleymans et al. [22]:  $T$  increases and  $\mu_B$  decreases monotonically with  $\sqrt{s_{NN}}$ , reflecting the transition from a baryon-rich, cooler freeze-out at lower energies to a baryon-dilute, hotter freeze-out at higher energies. The extracted temperatures are broadly consistent with lattice QCD estimates of the QCD crossover temperature  $T_c \approx 155$  MeV, particularly at higher  $\sqrt{s_{NN}}$  where  $\mu_B$  is small, placing the freeze-out conditions in the vicinity of the expected phase boundary.

Using the extracted  $T$  and  $\mu_B$ , we reconstructed the freeze-out trajectory in the net baryon density–energy density ( $\rho_B, \epsilon$ ) plane. Our results confirm the existence of a region of maximum net baryon density at intermediate energies ( $\sqrt{s_{NN}} \lesssim 11.5$  GeV), consistent with the expected onset of significant baryon stopping in this energy regime. Furthermore, we find that dynamical flow enhances the inferred compression:  $\rho_B$  at freeze-out is up to  $\sim 20\%$  higher in the dynamical scenario ( $v_z = 0.4$ ) compared to the static limit ( $v_z = 0$ ), underscoring the importance of accounting for collective motion when inferring thermodynamic conditions from spectra.

The integrated proton yields are found to be insensitive to  $v_z$ , which we attribute to two cooperating ef-

fects: first, the net-baryon content at mid-rapidity is established during the pre-equilibrium baryon stopping phase, before collective longitudinal flow develops; second, since the net-baryon rapidity distribution is broad and approximately flat near mid-rapidity at these energies, the rigid rapidity shift  $\Delta y \sim \tanh^{-1}(v_z)$  induced by longitudinal flow does not significantly alter the integrated yield within the narrow window  $|y| < 0.1$ . Pion yields, by contrast, increase monotonically with  $\sqrt{s_{NN}}$ , consistent with the transition from baryon-dominated to meson-dominated particle production as nuclear transparency increases with energy.

Several important extensions of the present work are envisaged. In the near term, the most pressing improvement is the inclusion of additional hadron species, in particular strange hadrons such as  $K^\pm$ ,  $\Lambda$ , and  $\Xi$ , in the simultaneous fit. This would allow the strangeness chemical potential  $\mu_S$  and the electric charge chemical potential  $\mu_Q$ , both set to zero in the present analysis, to be self-consistently determined. The latter is expected to be non-negligible at lower collision energies, where significant baryon stopping and the neutron-to-proton imbalance of the Au nucleus introduce an appreciable isospin asymmetry. A global multi-species fit would also provide a more robust test of the assumption of a single, common freeze-out surface for all particle species, which may break down if different species decouple from chemical equilibrium at different times. A self-consistent determination of the physically admissible range of  $v_z$  would require imposing  $T \leq T_c$  as a hard constraint in the fitting procedure. This would eliminate the unphysical high-temperature solutions currently admitted at large  $v_z$  and provide a more reliable determination of the longitudinal expansion velocity from  $p_T$  spectra alone.

Extending the analysis to wider rapidity windows would be particularly valuable for constraining  $v_z$  directly from data, as the insensitivity of mid-rapidity yields to longitudinal flow makes it impossible to determine  $v_z$  from spectra in the narrow  $|y| < 0.1$  window alone. Rapidity-differential spectra, combined with measurements of net-baryon rapidity distributions, would break this degeneracy and allow a precise extraction of the longitudinal expansion velocity.

Finally, while the present approach captures the freeze-out conditions through a parametrized velocity field at a single freeze-out surface, a more complete description would require coupling the statistical model to a full 3+1 dimensional viscous hydrodynamic evolution with a baryon-density-dependent equation of state (EoS). Such a framework would self-consistently link the development of collective flow to the underlying thermodynamic properties of the medium, in particular the speed of sound  $c_s^2 = \partial P / \partial \varepsilon$ , and would allow the freeze-out surface itself to be determined dynamically rather than imposed. Implementing such a model with an EoS that incorporates a QCD critical point would provide direct sensitivity to the conjectured first-order phase transition at large  $\mu_B$ , which is one of the primary physics motivations of the RHIC BES program. The freeze-out coordinates extracted in the present work provide an approximate estimates and benchmarks for such future hydrodynamic analyses.

## V. ACKNOWLEDGMENTS

V.R. acknowledges financial support from Anusandhan National Research Foundation (ANRF), India through Core Research Grant , CRG/2023/001309.

- 
- [1] Hitansh Shah, Mauricio Hippert, Jorge Noronha, Claudia Ratti, and Volodymyr Vovchenko. Locating the qcd critical point through contours of constant entropy density. *Phys. Rev. C*, 113:L012201, Jan 2026.
  - [2] Agnieszka Sorensen and Paul Sorensen. Locating the critical point for the hadron to quark-gluon plasma phase transition from finite-size scaling of proton cumulants in heavy-ion collisions. *arXiv*, 2405:10278, May 2024.
  - [3] Gokce Basar. On the qcd critical point, lee-yang edge singularities and pade resummations. *arXiv*, 2312:06952, July 2024.
  - [4] Roy A. Lacey. Indications for a critical end point in the phase diagram for hot and dense nuclear matter. *Phys. Rev. Lett.*, 114:142301, Apr 2015.
  - [5] D. A. Clarke, P. Dimopoulos, F. Di Renzo, J. Goswami, C. Schmidt, S. Singh, and K. Zambello. Searching for the qcd critical end point using multipoint padé approximations. *Phys. Rev. D*, 112:L091504, Nov 2025.
  - [6] Kazuyuki Kanaya, Ryo Ashikawa, Shinji Ejiri, Masakiyo Kitazawa, Hiroshi Suzuki, and Naoki Wakabayashi. Phase structure and critical point in heavy-quark qcd at finite temperature. *arXiv*, 2211:08631, November 2022.
  - [7] Y. Aoki, Z. Fodor, S.D. Katz, and K.K. Szabó. The qcd transition temperature: Results with physical masses in the continuum limit. *Physics Letters B*, 643(1):46–54, 2006.
  - [8] Anyi Li, Andrei Alexandru, and Keh-Fei Liu. Critical point of  $N_f=3$  qcd from lattice simulations in the canonical ensemble. *Phys. Rev. D*, 84:071503, Oct 2011.
  - [9] Adiba Shaikh, Ranjita K. Mohapatra, and Saumen Datta. Qcd phase diagram and the finite volume fireball: A model study. *Nuclear Physics A*, 1054:122981, 2025.
  - [10] Gergely Endrodi. Critical point in the qcd phase diagram for extremely strong background magnetic fields. *arXiv*, 1504:08280, July 2015.
  - [11] Eduardo S. Fraga, Letícia F. Palhares, and Paul Sorensen. Finite-size scaling as a tool in the search for the qcd critical point in heavy ion data. *Phys. Rev. C*, 84:011903, Jul 2011.
  - [12] S. Acharya et al. Closing in on critical net-baryon fluctuations at lhc energies: Cumulants up to third order in

- pb–pb collisions. *Physics Letters B*, 844:137545, 2023.
- [13] B. E. Aboona et al. Precision measurement of net-proton-number fluctuations in Au + Au collisions at rhic. *Phys. Rev. Lett.*, 135:142301, Sep 2025.
- [14] J. Randrup and J. Cleymans. Maximum freeze-out baryon density in nuclear collisions. *Phys. Rev. C*, 74:047901, Oct 2006.
- [15] A. Andronic, P. Braun-Munzinger, K. Redlich, and J. Stachel. Decoding the phase structure of qcd via particle production at high energy. *Nature*, 561:321–330, 2018.
- [16] Szabolcs Borsányi, Zoltán Fodor, Jana N. Guenther, Paolo Parotto, Attila Pásztor, Claudia Ratti, Volodymyr Vovchenko, and Chik Him Wong. Lattice qcd constraints on the critical point from an improved precision equation of state. *Phys. Rev. D*, 112:L111505, Dec 2025.
- [17] A. Bazavov, T. Bhattacharya, C. DeTar, H.-T. Ding, S. Gottlieb, R. Gupta, P. Hegde, U. M. Heller, F. Karsch, S. Mukherjee, P. Petreczky, C. Schmidt, R. A. Soltz, W. Soeldner, R. Sugar, M. Wagner, P. Vranas, et al. Equation of state in (2+1)-flavor qcd. *Phys. Rev. D*, 90:094503, 2014.
- [18] M. S. Abdallah et al. Measurements of proton high-order cumulants in  $\sqrt{s_{NN}} = 3$  GeV Au + Au collisions and implications for the qcd critical point. *Phys. Rev. Lett.*, 128:202303, May 2022.
- [19] Travis Dore, Jamie M. Karthein, Isaac Long, Debora Mroczek, Jacquelyn Noronha-Hostler, Paolo Parotto, Claudia Ratti, and Yukari Yamauchi. Critical lensing and kurtosis near a critical point in the qcd phase diagram in and out of equilibrium. *Phys. Rev. D*, 106:094024, Nov 2022.
- [20] B. Touschek. Covariant statistical mechanics. *Nuovo Cimento B*, 58:295, November 1968.
- [21] L Adamczyk et al. Bulk properties of the medium produced in relativistic heavy-ion collisions from the beam energy scan program. *Phys. Rev. C*, 96:044904, Oct 2017.
- [22] J. Cleymans, H. Oeschler, K. Redlich, and S. Wheaton. Comparison of chemical freeze-out criteria in heavy-ion collisions. *Phys. Rev. C*, 73:034905, Mar 2006.